Second-Harmonic Ripple Voltage Suppression of Integrated Single-Phase PWM Rectifier Charging System for EVs

Yun Zhang, *Senior Member, IEEE*, Jian Fang, Fei Gao, *Member, IEEE*, Tianbao Song, Shenghan Gao, and Daniel Rogers, *Senior Member, IEEE*

***Abstract*- In single-phase AC battery chargers, pulsating power at twice of the line frequency is delivered by the AC source resulting in second-harmonic ripple voltage on the DC-link if additional passive or active filter circuits are not used. In this paper, an inductance-based active filter (AF) using the leakage inductance of the machine windings along with a current compensation control method is proposed. No additional passive components are required. The machine used in this paper has a double-layer winding with a center tap in each phase and the winding structure of the machine is special in that the pulsating magnetomotive force of the whole phase winding can be cancelled when currents flow into the central tap. In this paper, the operating principle and control strategy of the AF with the inductive energy storage are analyzed. Finally, a 400W experimental prototype is developed and the experimental results are used to validate the performance and feasibility of the proposed converter and control strategy.**

***Index Terms*—Active filter (AF), current compensation control, integrated charging system, inductive energy storage, center-tapped winding, second-harmonic ripple voltage, single-phase Pulse-Width Modulation (PWM) rectifier**

I. INTRODUCTION

Electric vehicles powered by renewable energy achieve clean, carbon-neutral operation and are one of the new modes of transportation that will help alleviate the pressures on energy resources reduce environmental pollution [1], [2]. EV charging systems have recently received attention in the literature [3]-[5]. Fig.2 shows the structure of an integrated charging system (i.e. a charging system that is built into the vehicle). EV charging may be divided into three-phase fast charging (high power) and single-phase slow charging (lower power). For most household EVs, only single-phase slow charging is generally adopted due to supply availability. Slow charging has an additional benefit of prolonging battery service life [6]. In order to provide controllable charging voltage and current for high-voltage batteries, and ensure that the AC-link power factor is controllable and energy can flow in both directions, single-phase PWM fully-controllable converters are widely applied. In both rectification and inverter mode, the single-phase PWM rectifier can constrain the AC-side current to the same frequency and phase as the grid voltage, so that the system obtains a unity power factor. However, a pulsating input power at twice the frequency of the grid voltage is generated from the combined action of sinusoidal alternating current and grid voltage, and the average value of the pulsating AC input power is equal to the DC output power (neglecting losses), which is shown in Fig.1 [7]. For EV charging systems, the second-harmonic pulsating current is potentially harmful to the batteries, as it can produce additional electrochemical overpotential at high states of charge, as well as causing temperature rise due to higher RMS current, resulting in shorter battery life [8], [9]. Generally, the ripple current of battery should be less than 10% of its rated value [10]. Therefore, to suppress the second-harmonic ripple voltage generated in DC side of single-phase PWM rectifier in the integrated charging system is of great importance [11]-[13]. So far, there are two dominant methods to suppress the second-harmonic ripple voltage: passive filtering and active filtering.

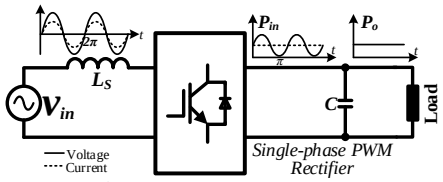


Fig.1 The generation of second harmonic power in single-phase PWM rectifier.

Large DC capacitors or LC resonant circuits connected in parallel with the DC bus are the two main methods of passive filtering to suppress the second-harmonic ripple voltage. The former method is simple and effective, but limits the overall power density of highly integrated power converters. The latter improves power density to a certain extent, but is sensitive to parameters offset so that improper parameter selection can result in resonance of the system, as well as large second-harmonic current between the supporting capacitor and the LC resonant circuit on the DC side.

In order to eliminate the second-harmonic ripple voltage and improve the power density of the single-phase PWM rectifier charging system, many methods of active filtering have been proposed in the literature. Active filters (AFs) can be divided into depending on whether the AF is on the DC-link side [14]-[15] or on the AC-link side. Another division can be made based on whether the AF uses capacitive [16]-[17] or inductive energy storage [18]-[20]. For DC-link AF, bidirectional DC-DC converters with energy storage units are typically paralleled on the DC side of the single-phase PWM converter. Unlike the passive filter with paralleled LC resonant circuits, the DC-link AF is usually connected to the DC bus by a bidirectional DC-DC converter. Thus the DC bus

Manuscript received Dec. 25, 2018; accepted Aug. 23, 2019. This work was supported by the National Natural Science Foundation of China under Grants 51577130 and 51977145.

Y. Zhang, J. Fang , T. Song and S. Gao are with the School of Electrical and Information Engineering, Tianjin University, Nankai, Tianjin, China (e-mail: zhangy@tju.edu.cn; fangjianjack@163.com; 1244385687@qq.com; 18811757258@163.com).

F. Gao is with the Department of Electrical Engineering, Shanghai Jiao Tong University, Shanghai, China (email: sjtugf@163.com;).

D. J. Rogers is with the Department of Engineering Science , University of Oxford, UK. (email: dan.rogers@eng.ox.ac.uk).

will not be affected even if the capacitor voltage or inductor current of the DC-DC converter fluctuates over a wide range. Capacitors typically provide much higher energy storage density than inductors and so are often favored for AFs if a separate discrete energy component must be selected [21], [22].

However, scholars have reported performing AF by exploiting the independence of traction mode and charging mode in the integrated electric drive system of EVs [23], [24], i.e. using the observation that EVs are generally not charged while they are moving. In other words, components of the EV that traditionally operate only in traction mode can be reused for charging when the vehicle is stationary. In [25], the auxiliary power module in the integrated electric drive system of EVs is adopted, namely, the active filter operated on the DC side of a single-phase PFC converter is composed of an isolated dual active bridge bidirectional DC-DC converter and an energy storage element. Although it can suppress the second-harmonic ripple voltage without additional bidirectional DC-DC converters, this method requires additional energy storage components and so does not achieve complete integration.

An integrated single-phase charging system for EVs is proposed in [26] and [27]. In [27], the machine winding is used as the filter inductor on the AC input side for the single-phase charging. However, due to the use of a dual three-phase winding machine, an additional winding current balance control algorithm is required to eliminate the pulsating and rotating magnetomotive forces that are generated by the current flowing through the winding in charging mode.

To-date, AF performed on the DC side using the machine windings as an energy storage has not yet been explored in the literature. In this paper, an AF with the inductive energy storage based on the integrated charging system for EVs is proposed. This AF suppresses the second-harmonic ripple voltage in the single-phase PWM converter charging system. The leakage inductance of center-tapped double-layer windings in the three-phase machine as well as the filter inductor in the single-phase PWM rectifier is used as the energy storage element in the AF. As a result, no additional winding current balance control algorithm is needed to eliminate the pulsating and rotating magnetomotive forces. As the system contains very few additional components or circuits, the proposed integrated AF with the inductive energy storage can realize higher power density and integration. In addition, this paper proposes a current compensation control method based on the external voltage loop of the single-phase PWM rectifier, which can make a further contribution to the suppression of the second-harmonic pulsating power.

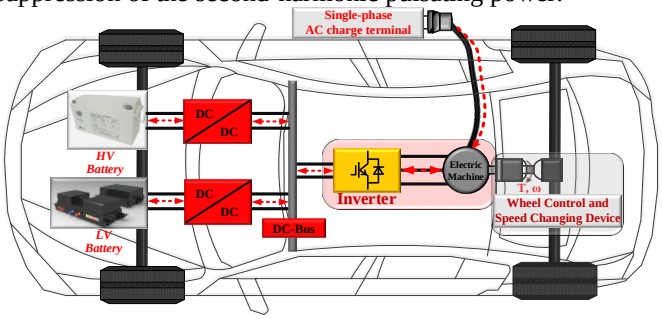


Fig.2. Structure diagram of integrated charging system for EV.

The structure of the paper is organized as follows. Section II introduces the proposed integrated charging converter with the second-harmonic ripple voltage suppression, then analyzes the operation principle of the proposed converter and describes the model of the traction machine with center-tapped double-layer windings. Section III presents the principle of the second-harmonic ripple voltage suppression and its control strategy. The experiment results and detailed discussions are shown in Section IV. Finally, Section V draws the conclusion.

II. PROPOSED INTEGRATED CONVERTER FOR SECOND-HARMONIC RIPPLE VOLTAGE SUPPRESSION METHOD

The converter can operate in either traction mode or charging mode by reusing the machine windings in the charging system. In the charging mode, a three-phase AC source can be used for fast charging, and also a single-phase AC source can be used for slow charging. Fig.3 shows the configuration of the single-phase integrated charging system.

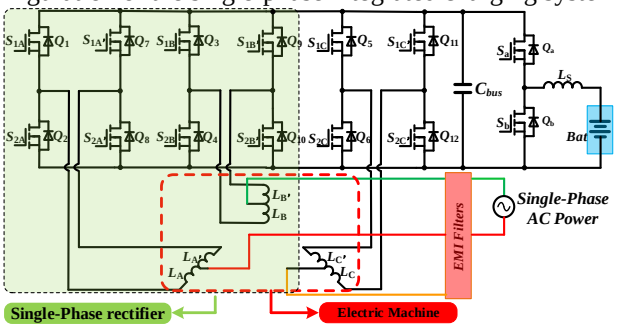


Fig.3. Configuration of the single-phase integrated charging system.

A. *Operating principle of the proposed converter*

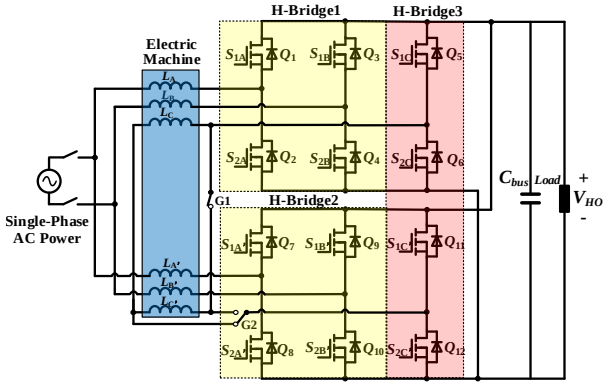


Fig.4. Proposed charging system with second-harmonic ripple voltage suppression. Relays G_1 and G_2 shown in the on (charging) position.

The configuration of the proposed charging system with the second-harmonic ripple voltage suppression is shown in Fig.4. As it can be seen from Fig.4, the converter is composed of three H-Bridges with a common DC bus, and a three-phase induction machine with center-tapped double-layer windings. As illustrated, the system operates in a single-phase charging mode. Of the three H-Bridges, two of them (H-Bridge1 and H-Bridge2) are input-parallel and output-parallel, while the leakage inductances L_{kA} of L_A, $L_{A'}$ and L_{kB} of L_B, $L_{B'}$ provided by the three-phase machine windings are used as filter inductors, which causes both H-Bridges operate in parallel in the single-phase PWM rectifier mode. The second-harmonic ripple voltage is generated by the single-phase PWM rectifier and is corrected by the AF utilizing the leakage inductance L_k

of the machine windings (L_C and $L_{C'}$) and the third H-bridge (H-Bridge3), without adding any additional energy storage components or circuits. Through the operation of relays G_1 and G_2, the system can be switched between charging and traction modes: the system operates in the charging mode when relays G_1 and G_2 are both turned on and operates in the traction mode when relays G_1 and G_2 are both turned off.

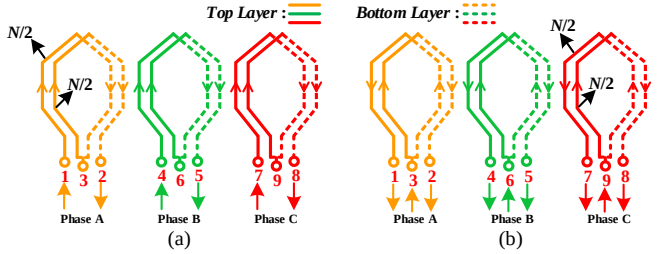


Fig.5. Distribution diagram in the slot of three-phase double-layer windings with a central tap.(a) Traction mode. (b) Charging mode.

B. Model of three-phase traction machine with center-tapped double-layer winding

A high level of integration between traction and charging systems is achieved by using a three-phase induction machine with center-tapped double-layer winding. The two armature windings of each phase are located in the upper and lower layers of the same slot in the iron core, and the total turns N on the top and bottom layers can be divided into the two equal parts (i.e. $N/2$ respectively), as shown in Fig.5.

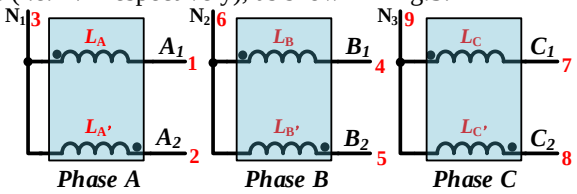


Fig.6. Winding connections.

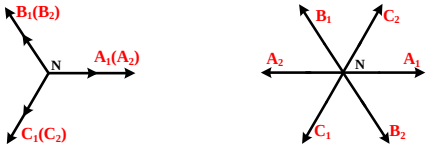


Fig.7. Star diagrams of magnetomotive force for each phase. (a) Traction mode. (b) Charging mode.

The winding structure of the machine must be modified from that of a conventional three-phase star or delta connected machine in order to enable its use as the energy storage element in the proposed AF. The machine must be constructed with center-tapped double-layer windings, and it is assumed that each phase winding and its split parts are balanced, in order to eliminate the pulsating magnetomotive force and the resulting electromagnetic torque on the rotor. For a center-tapped double-layer winding machine, the magnetomotive force of each phase is synthesized by two split stator coils, which can be seen in Fig.5. The winding connections are shown in Fig.6. It can be seen from the diagram that when the current flows into the central tap, A_1 and A_2 (B_1 and B_2, C_1 and C_2) belong to the same phase winding and so their magnetomotive forces are opposite in directions and cancel each other out. As a result there is no net pulsating magnetomotive force produced by any phase and so no rotating magnetomotive force in the machine. Critically, although the self-inductance of the whole winding is zero, the leakage inductance still exists according to Fig.5 and Fig.6. Fig.7 (a) and Fig.7 (b) represent the star diagrams of magnetomotive force in each phase in the charging and traction modes, respectively. Fig.7 (b) shows that in the traction mode, this connection manner allows the machine to obtain the maximum synthetic magnetomotive force in each phase. It is important to note that although the inverter design proposed in this paper requires 12 power switches (connected as three H-bridges) compared to the six switches of a conventional three phase bridge circuit, the total apparent power rating of the semiconductor devices is the same in both cases.

To illustrate this, consider two machines with an identical number of turns on each phase of the stator winding; one machine is a conventional machine and the other is a machine with the center-tapped winding structure proposed here. The DC bus voltage of the proposed inverter will be halved because each bridge is connected from the end of the winding to the center tap, instead of end-to-end as in the conventional case. As a result, the voltage stress across the power switches is halved but the overall power rating of the each system is identical.

III. SECOND-HARMONIC RIPPLE VOLTAGE SUPPRESSION

A. Principle of Second-harmonic Ripple Voltage Suppression

Fig.8 shows an equivalent circuit with the second-harmonic ripple voltage suppression in the integrated charging system, which consists of an H-Bridge (H-Bridge3) and an equivalent leakage inductor L_k. The inductor L_k can play a role of "peak shaving and valley filling" in the process of suppressing low-frequency pulsating power as follows: it absorbs energy when the instantaneous output power is greater than the average output power. When the instantaneous output power is less than the average output power, it releases the stored energy to compensate for the power shortage. Thus, there will be no fluctuations of the output voltage and current on the DC side.

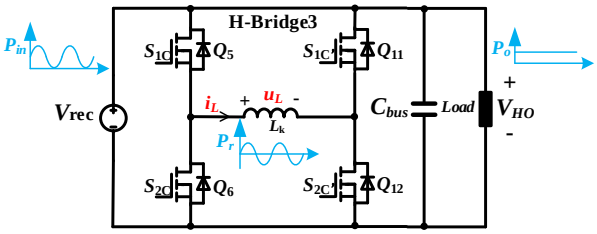


Fig.8. Equivalent circuit with second-harmonic ripple voltage suppression (the instantaneous power difference between AC and DC sides is supplied by the active filter).

As shown in Fig.8, the inductor current can be controlled because the converter is symmetrical. Namely, the inductor current can flow either in DC mode or in AC mode. Since the machine winding is a magnetic component, when the current flows in DC mode, the DC component will cause a DC flux bias, potentially resulting in magnetic saturation. However, it can be avoided when the inductor current flows in AC mode. The schematic diagrams of the inductor current in DC and AC modes are shown in Fig.9 and Fig.10 respectively.

It can be seen from Fig.8 and Fig.9 that the gate signals S_{1C} and $S_{2C'}$ of the power switches Q_5 and Q_{12} are identical, so do the gate signals S_{2C} and $S_{1C'}$ of the power switches Q_6 and Q_{11} .That is to say, they are turned on and off at the same time in complimentary pairs. In Fig.8, power switches Q_5 and Q_{12} are turned on and Q_6 and Q_{11} are turned off while the inductor is storing energy. When the energy is released from the inductor, the current flows through the anti-parallel diodes of Q_6 and Q_{11}. Synchronous operation is employed in order to reduce conduction losses.

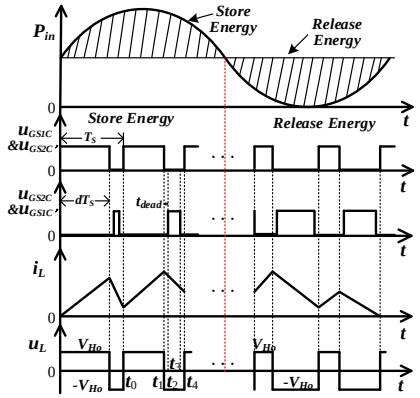


Fig.9. Schematic diagram of the inductor current flowing in DC mode.

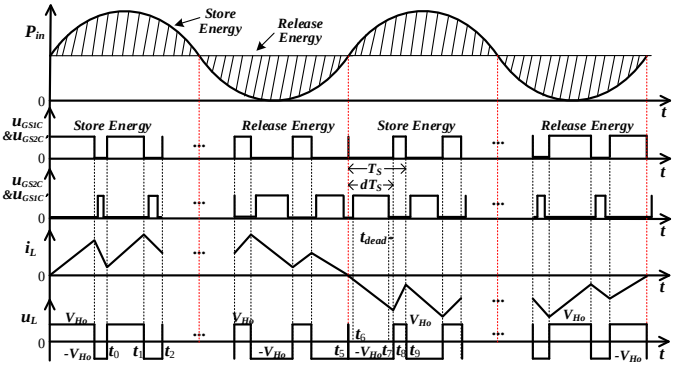


Fig.10. Schematic diagram of the inductor current flowing in AC mode.

To simplify the analysis, all components are assumed to be ideal, for example by neglecting the on-state resistance R_{DS}(on) of the power switches and equivalent series resistance (ESR) of the inductors and capacitors. In addition, the inductor (i.e. traction machine) is assumed to behave linearly (saturation is not modelled). The reference direction of the inductor current and voltage are shown in Fig.8.

It can be seen from Fig.9 that there are four operating states for the converter during one switching period when the inductor current flows in DC mode (inductor current positive or zero). The corresponding current flow paths are illustrated in Fig.11 and are described as follows:

State0 **[t_0-t_1]:** When $S_{1C}S_{2C}S_{1C'}S_{2C'}$=1001, Q_5 and Q_{12} are turned on, Q_6 and Q_{11} are turned off, the current flow paths are shown in Fig.11 (a). In this time, the inductor absorbs energy via Q_5 and Q_{12}. The inductor current increases positively and the voltage across the inductor is equal to V_{HO}.

State1 **[t_1-t_2]:** When $S_{1C}S_{2C}S_{1C'}S_{2C'}$=0000, Q_5, Q_6, Q_{11} and Q_{12} are turned off, and the anti-parallel diodes of Q_6 and Q_{11} are turned on because the direction of the inductor current cannot change suddenly. The current flow paths are shown in Fig.11 (b). The inductor releases energy through the anti-parallel diodes. The inductor current decreases positively and the voltage across the inductor is equal to -V_{HO}.

State2 **[t_2-t_3]:** When $S_{1C}S_{2C}S_{1C'}S_{2C'}$=0110, Q_6 and Q_{11} are turned on, Q_5 and Q_{12} are turned off, the current flow paths are shown in Fig.11 (c). The inductor releases energy through Q_6 and Q_{11}. The inductor current decreases positively, while the voltage across the inductor is equal to -V_{HO}.

State3 **[t_3-t_4]:** Equivalent to *State1*.

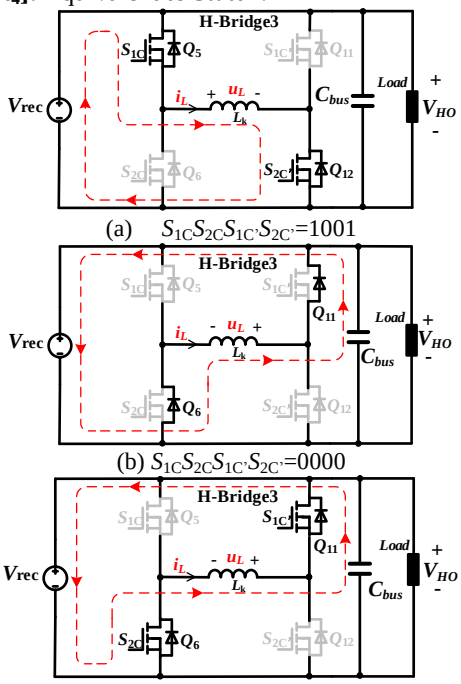


Fig.11. Current flow paths when it operates in DC mode.

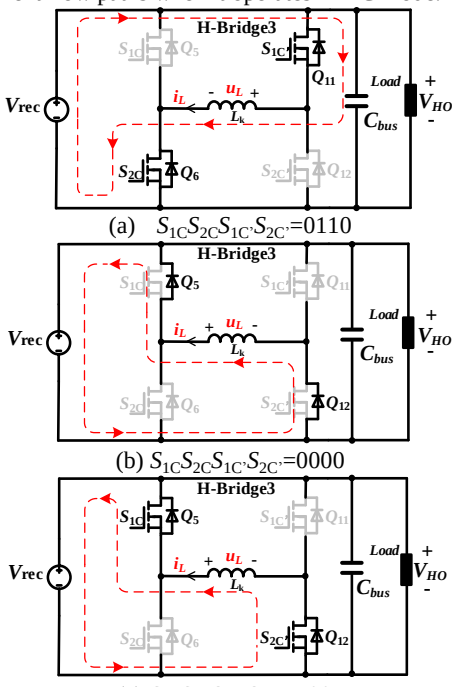


Fig.12. Current flow paths when it operates in AC mode.

As shown in Fig.10, the inductor may be operated in AC mode, that is, inductor current is positive during one period of the instantaneous input power and negative during the next period. Thus, a symmetric AC inductor current is formed. This helps avoid possible problems that could result from applying

a DC bias flux in the traction machine. In AC mode, in addition to the four operating states and the current flow paths of DC mode, there are four further operating states with the corresponding current flow paths as follows:

***State4* [t_5-t_6]:** When $S_{1C}S_{2C}S_{1C'}S_{2C'}$=0110, Q_6 and Q_{11} are turned on, Q_5 and Q_{12} are turned off, the current flow paths are shown in Fig.12 (a). The inductor stores energy via Q_6 and Q_{11}. The inductor current increases negatively, while the voltage across the inductor is equal to $-V_{HO}$.

***State5* [t_6-t_7]:** When $S_{1C}S_{2C}S_{1C'}S_{2C'}$=0000, Q_5, Q_6, Q_{11} and Q_{12} are turned off, and the anti-parallel diodes of Q_5 and Q_{12} are turned on because of the direction of inductor current cannot change suddenly. The current flow paths are shown in Fig.12 (b). The inductor releases energy through the anti-parallel diodes. The inductor current decreases negatively and the voltage across the inductor is equal to $-V_{HO}$.

***State6* [t_7-t_8]:** When $S_{1C}S_{2C}S_{1C'}S_{2C'}$=1001, Q_5 and Q_{12} are turned on, Q_6 and Q_{11} are turned off, the current flow paths are shown in Fig.12 (c). The inductor releases energy through Q_5 and Q_{12}. The inductor current decreases negatively and the voltage across the inductor is equal to V_{HO}.

***State7* [t_8-t_9]:** Equivalent to *State5*.

B. Control Strategy

First of all, a simple quantitative analysis of second-harmonic pulsating power produced in single-phase PWM rectifier is carried out, in order to further illustrate the control strategy adopted in this paper.

Assuming that the sinusoidal input AC voltage u_s and the sinusoidal input AC current i_s are not distorted, the expression is as shown in equation (1), with the power factor of the single-phase PWM rectifier is considered to be 1,

$$\begin{cases} u_s(t) = V_S \cdot \sin(\omega t) \\ i_s(t) = I_S \cdot \sin(\omega t) \end{cases} \tag{1}$$

where V_S and I_S are the magnitudes of grid voltage and input current respectively, and ω is the angular frequency.

According to (1), the instantaneous input power on the AC side of the single-phase PWM rectifier can be derived as

$$p_s(t) = u_s(t) \cdot i_s(t) = \frac{V_S I_S}{2} - \frac{V_S I_S}{2}\cos(2\omega t) \tag{2}$$

The input filter inductor L is the equivalent leakage inductance of L_A, $L_{A'}$ and L_B, $L_{B'}$, and the instantaneous power it absorbed is

$$p_L(t) = L \cdot \frac{di_s(t)}{dt} \cdot i_s(t) = \frac{\omega L I_S^2}{2}\sin(2\omega t) \tag{3}$$

Then, the total instantaneous input power of the rectifier can be obtained as

$$\begin{aligned} p_{\text{in}}(t) &= p_s(t) - p_L(t) \\ &= \frac{V_S I_S}{2} - \frac{V_S I_S}{2}\cos(2\omega t) - \frac{\omega L I_S^2}{2}\sin(2\omega t) \end{aligned} \tag{4}$$

$$p_o(t) = \frac{V_S I_S}{2} \tag{5}$$

$$\begin{aligned} p_r(t) &= -\frac{V_S I_S}{2}\cos(2\omega t) - \frac{\omega L I_S^2}{2}\sin(2\omega t) \\ &= -p_{r_peak}\sin(2\omega t + \psi) \end{aligned} \tag{6}$$

where $p_o(t)$ is the instantaneous average output power, which is the DC component of $p_{in}(t)$, namely the active power component; $p_r(t)$ is the second-harmonic pulsating power, which is the AC component of $p_{in}(t)$, namely the reactive power component. In (6), the amplitude p_{r_peak} of the second-harmonic pulsating power with its phase angle ψ can be obtained as

$$\begin{cases} p_{r_peak} = \sqrt{V_S^2 I_S^2 + \omega^2 L^2 I_S^4}/2 \\ \psi \quad = \tan^{-1}(V_S / \omega L I_S) \end{cases} \tag{7}$$

1) Reference current in DC mode. The instantaneous power transferred from DC bus to the inductor is obtained as

$$p_r(t) = u_L(t) \cdot i_{L1}(t) = L_k \cdot \frac{di_{L1}(t)}{dt} \cdot i_{L1}(t) \tag{8}$$

where $u_L(t)$ and $i_{L1}(t)$ are the instantaneous voltage and current of inductor L_k respectively. The reference current of the inductor can be derived from (6) and (8) as

$$i_{L1}(t) = \sqrt{\frac{p_{r_peak}}{\omega L_k}[\cos(2\omega t + \psi) - \cos\psi + K]} \tag{9}$$

where K is the constant in the integration calculation, whose physical meaning is related to the peak value of the inductor current I_{L1_max}, and it can be obtained as

$$K = \frac{\omega L_k I_{L1_\max}^2}{p_{r_peak}} + \cos\psi - 1 \tag{10}$$

The energy stored in inductor at each time can be written as

$$\begin{cases} \frac{1}{2}L_k I_{L1_\max}^2 - \frac{1}{2}L_k I_{L1_\min}^2 = W_{L1} \\ W_{L1} = \frac{p_{r_peak}}{\omega} \end{cases} \tag{11}$$

where I_{L1_min} is the minimum value of the inductor current that satisfies $I_{L1_max} > I_{L1_min} \geq 0$, and W_{L1} is the stored energy of the inductor. Therefore, the maximum value of the inductor current can be derived as

$$I_{L1_\max} = \sqrt{\frac{2p_{r_peak}}{\omega L_k} + I_{L1_\min}^2} \tag{12}$$

The peak value of the inductor current can reach its minimum value when I_{L1_min} is equal to 0, and at this time $K = 1 + \cos\psi$. Thus the range of K can be obtained as

$$K \geq 1 + \cos\psi \tag{13}$$

2) Reference current in AC mode. Assuming that the reference inductor current can be defined as

$$i_{L2}(t) = I_{L2_peak}\sin(\omega t + \varphi) \tag{14}$$

where I_{L2_peak} is the peak value of the inductor current and φ is the phase angle. The instantaneous voltage across the inductor can be obtained as

$$u_{L2}(t) = L_k \frac{di_{L2}(t)}{dt} = \omega L_k I_{L2_peak}\cos(\omega t + \varphi) \tag{15}$$

According to (14) and (15), the instantaneous power of the inductor L_k is given by

$$p_{L2}(t) = u_{L2}(t) i_{L2}(t) = \frac{1}{2}\omega L_k I_{L2_peak}^2 \sin(2\omega t + 2\varphi) \tag{16}$$

When the instantaneous power $p_{L2}(t)$ stored in the inductor is equal to the instantaneous pulsating power $p_r(t)$ at two times of the grid frequency, according to (6) and (16), the peak value

of the inductor current I_{L2_peak} and the phase angle φ can be obtained as

$$\begin{cases} I_{L_peak} = \sqrt{\dfrac{2p_{r_peak}}{\omega L_k}} \\ \varphi = \dfrac{\pi}{2} + \dfrac{\psi}{2} \end{cases} \tag{17}$$

So, the reference current in AC mode can be given from the following

$$\begin{cases} i_{L2}(t) = \sqrt{\dfrac{2p_{r_peak}}{\omega L_k}} \sin(\omega t + \varphi) \\ \varphi = \dfrac{\pi}{2} + \dfrac{\psi}{2} \end{cases} \tag{18}$$

The inductor L_k absorbs and releases energy by controlling its current as (9) or (18), so that, theoretically, second-harmonic pulsating power suppression is achieved completely.

It can be seen from Fig.9 that the switching period of the filter is T_S, the duty cycle of Q_5 and Q_{12} is d, and the duty cycle of Q_6 and Q_{11} is (1-d). According to the volt-second balance principle, that is

$$u_L T_S = dT_S V_{HO} - (1-d)T_S V_{HO}\,, \tag{19}$$

the duty cycle in each switching period can be obtained as follows

$$d = \frac{u_L}{2V_{HO}} + \frac{1}{2}\quad . \tag{20}$$

As a result, the control block diagram of the converter with the second-harmonic pulsating power suppression can be obtained as shown in Fig.13.

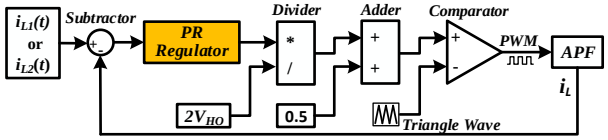


Fig.13. Control block diagram of the converter with second-harmonic pulsating power suppression.

It can be seen that this control strategy uses a single current loop based on a PR (Proportional-Resonant) regulator. It is necessary to track an alternating value when the current flows in AC mode. Typically in this type of application the PR regulator has a better performance than that of a PI regulator. The second-harmonic pulsating power is suppressed by regulating the inductor current and making it equal to the reference value.

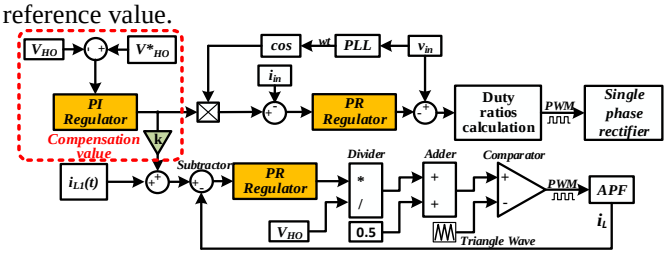


Fig.14. Control block diagram of AF with current compensation control strategy.

The losses of the equivalent resistors and the power switches are ignored in the previous calculation of the reference inductor current. However, in practical applications, these losses will cause inaccuracy in the previous calculation. Hence, a current compensation control strategy using a DC-link voltage loop is proposed. The corresponding control block diagram is shown in Fig.14, where k is a tunable correction parameter. The output value of the voltage loop tends to increase the value of the reference inductor current in the AF, which compensates for power losses in the power switches and passive components.

3) Analysis of the leakage inductance, charging/traction power and current stress on the power device. For the previous circuits shown in Fig.4 and Fig.8, according to the principle of conservation of energy, the relationship among the single-phase charging power P, energy storage inductance (machine winding) L_k and current stress I_{L_max} of power switch can be obtained as

$$\begin{cases} \dfrac{1}{2} L_k I_{L_\max}^2 = \dfrac{P}{\omega} \\ I_{L_rms} = \dfrac{I_{L_\max}}{\sqrt{2}} \end{cases} \tag{21}$$

Similarly, the relationship among the rated power of machine P_m, the three-phase rated input voltage $U_{\varphi N}$, the base impedance Z_b, the leakage reactance X_σ and the leakage inductance L_k can be obtained as follows:

$$\begin{cases} Z_b = \dfrac{U_{\varphi N}^2}{P_m} \\ X_\sigma = 0.1 Z_b \\ L_k = \dfrac{1}{2} \cdot \dfrac{X_\sigma}{\omega} \end{cases} \tag{22}$$

It can be seen from (21) that leakage inductance (depending on the rated power of the traction machine) is inversely proportional to the square of the peak current flowing through the winding, when the charging power is constant. According to (21) and (22), Fig.15 and Fig.16 can be obtained, where $U_{\varphi N}$=380 V, P=3.3 kW, f=50 Hz, and noting that the unit value of the leakage reactance X_σ is typically about 0.1 [28]. Considering the acceleration process of EVs, the machine can overload 60% in a short time, and the excellent heat dissipation system can make the running time longer. Therefore, Fig.15 shows the relationship among the current stress of the switching device, the rated current of the winding and the rated power of the machine in the traction and charging modes. It can be seen that the current-flowing capacity of the winding in charging mode is within the range of traction mode, when the rated power of machine is over 19.3 kW, but the current stress of the switching device in the charging mode is larger than that in the traction mode, when it is below 77 kW, and the relationship between them is opposite when it is over 77 kW. The magnitude of the input filter and the energy storage inductances in machines with different rated power levels are shown in Fig.16. As it can be seen that the inductances are increased with the decreasing of the rated power of the machine, and thus the current stress of the switching device becomes smaller in the charging mode.

As an example of EV application, it is assumed that the rated power of the traction machine is 20 kW ($U_{\varphi N}$ =380 V, $I_{\varphi N}$=30 A at 50 Hz). Therefore the impedance of each phase winding is 7.22 Ω, the leakage inductance of the winding in AF is 1.2 mH. Thus, the RMS value of the current flowing through the energy storage inductance in AF is 93.6 A by (21)

and (22). As a result, the RMS value of the current flowing in each of the double-layer windings is 93.6/2=46.8 A. And the current-flowing capacity of the winding in traction mode is 30×1.6=48 A. This is close to the rating current 46.8 A of the machine winding in the charging mode. The input filter inductance in the single-phase PWM rectifier is 2.4 mH (For each independent H-bridge rectifier), and it can satisfy the design requirement of the filter inductance.

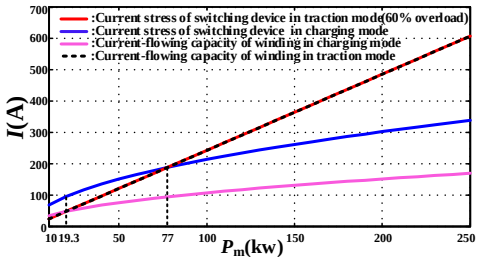


Fig.15. Currents through winding and power device in charging/traction mode under different power levels of machines.

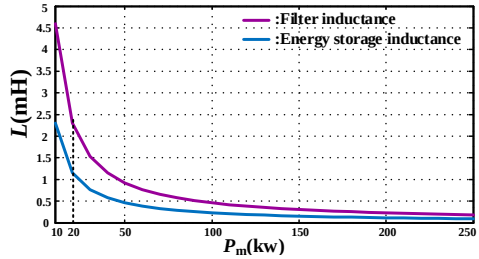


Fig.16. Filtering and energy storage inductances under different power levels of machines.

IV. EXPERIMENTAL RESULTS

In order to validate the effectiveness of the proposed converter and its control strategy, a scaled-down experimental prototype was developed. The leakage inductance of the machine winding was simulated by using reactors in the input filter inductor and as the energy storage inductor on the DC side. Based on the single-phase/three-phase integrated charging experimental platform with an additional H-Bridge, a 400W prototype with 100V_{rms} input voltage, 200V DC bus voltage, and 100Ω load resistance was developed, as shown in Fig.17.

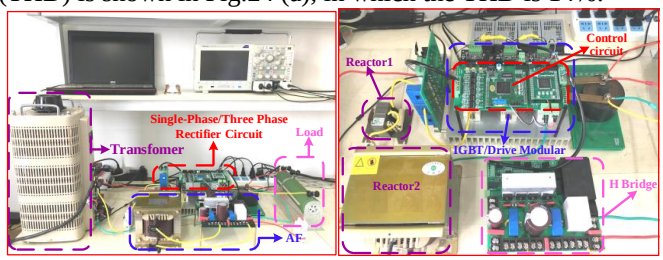
TABLE I Experimental parameters of integrated charging system

Modular	*Parameter*	*Values*
Single-Phase PWM Rectifier	Amplitude of grid voltage: U_S	141V
	Angular frequency of grid: ω	100π rad/s
	DC bus voltage: V_{HO}	200V
	Filtering capacitor in DC-link: C	200μF
	Filtering inductor in AC-link: L_S	5mH
	Switching frequency: f_s	10kHz
	Load resistance: R	100Ω
AF with inductive energy storage	Energy storage inductor: L_k	20mH
	Switching frequency: f_{s1}	20kHz

The specific parameters of the experimental prototype are listed in TABLE I. The Texas Instruments microcontroller TMS320F28335 (DSP) and ALTERA microcontroller EP4CE622C8N (FPGA) are used to implement the current and voltage loop controllers. The H-Bridge in the single-phase rectifier uses an Infineon FF50R12RT4 IGBT module.

A. Steady-state Performance

For the sake of comparison with the effect of the proposed inductive energy storage AF, the experimental results of a 400-W single-phase PWM rectifier are shown in Fig.18 as a benchmark, whose secondary voltage of the transformer is 100 V_{rms} and the line frequency is 50Hz. The input AC current is in phase with the input AC voltage approximately. However, the peak-to-peak value of the second-harmonic ripple voltage on the DC bus is 52V, i.e. its ripple is 26%. Thus, the input AC current is distorted due to the large ripple voltage on the DC side. The experimental result of the total harmonic distortion (THD) is shown in Fig.24 (a), in which the THD is 14%.



(a) (b)

Fig.17. Prototype of the proposed converter. (a) Overview of the system. (b) Detailed part of the system.

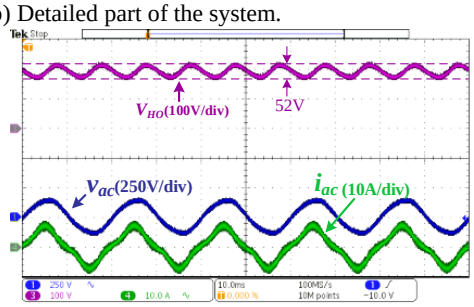


Fig.18. Experimental result of single-phase PWM rectifier without AF operation in integrated charging system.

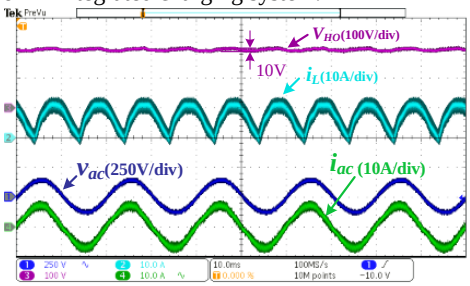


Fig.19. Experimental result of single-phase PWM rectifier with AF operation in integrated charging system when the inductor current flows in DC mode.

Fig.19 shows the experimental results of the single-phase rectifier charging with the AF operation when the inductor current flows in DC mode. A 20-mH reactor is applied as the energy storage inductor; its peak current value is 12A and the average voltage in the DC-link is 200V. Meanwhile, the second-harmonic ripple voltage can be reduced to 10V, i.e. its ripple voltage is reduced to 5%, demonstrating second-harmonic ripple voltage suppression. Also, the quality of the input AC current is improved as shown in Fig.24 (b), in which the THD is 3.4%.

The experimental result of the single-phase PWM rectifier with the AF operation and the current compensation control in the integrated charging system is shown in Fig.20. It can be seen from Fig.20 that the current compensation value is 1A and the peak value of the inductor current is 13A. Meanwhile, the second-harmonic ripple voltage is reduced to 8V and its ripple is reduced to 4%. Compared with the experimental results above (see Fig. 19), the second-harmonic ripple voltage is further reduced by 20% after employing current compensation control.

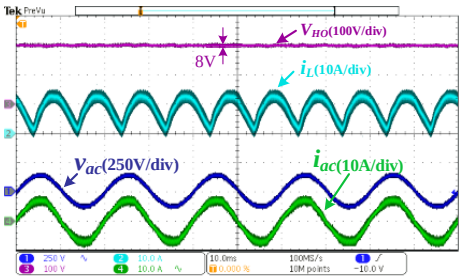


Fig.20. Experimental result of single-phase PWM rectifier with AF operation and its current compensation control method in integrated charging system.

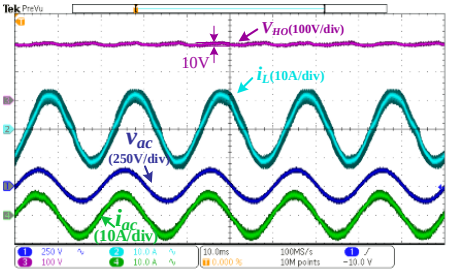


Fig.21. Experimental result of single-phase PWM rectifier with AF operation in integrated charging system when the inductor current flows in AC mode.

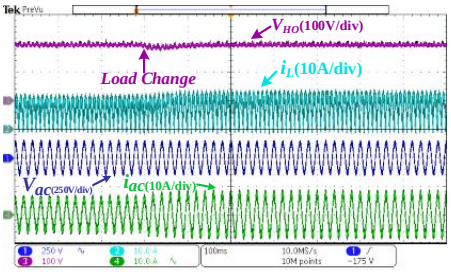


Fig.22. Experimental result of load step change from 133Ω to 100Ω.

Fig.21 shows the experimental results of the single-phase PWM rectifier with AF operation in the integrated charging system when the inductor current flows in AC mode, and the secondary voltage of the transformer is 100 V_{rms}. The frequency of the inductor current is 50Hz and its peak value is 12A, and the average DC-link voltage is 200V. It should be noted that there is no DC component in the inductor current comparing with that in Fig.20, which in turn avoids the magnetic saturation effect caused by the DC bias. At the same time, the second-harmonic ripple voltage is 10V, which is similar to that when the inductor current flows in DC mode.

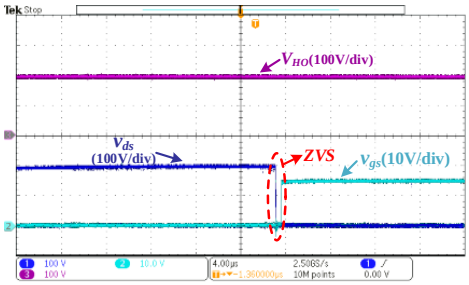
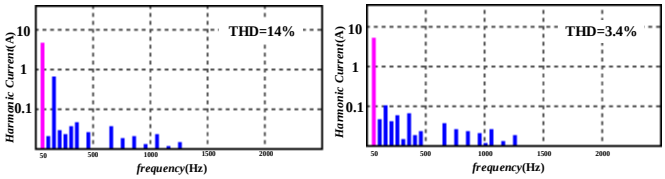


Fig.23. Voltage stress across the high frequency power switch with P_o=100W, V_{HO}=200V showing ZVS for Q_6.

The voltage stress occurring across the high frequency power switch is shown in Fig. 23. Zero voltage switching (ZVS) can be achieved for Q_6 as it operates under synchronous rectification. It can be seen that the voltage stress is equal to the DC bus voltage V_{HO}.

B. Transient Performance

In order to validate the dynamic performance of the proposed integrated charging system with the second-harmonic ripple voltage suppression, the experimental results of the load step change from 133Ω to 100Ω, i.e. the power is changing from 300W to 400W as shown in Fig.22. It can be seen that, the DC bus voltage quickly reaches steady state in less than 100ms.



(a) (b)

Fig.24. Fourier analysis of the input current. (a) Without AF. (b) With AF.

V. Conclusion

This paper has presented an active filter to suppress second-harmonic ripple voltage generated by a single-phase charging system. The active filter uses the leakage inductance of a modified EV traction machine as an energy storage element, thereby eliminating the need for a bulky and expensive filter capacitor and/or inductor. As a result, significant cost savings and power density improvements may be made in the charger circuit when this concept is applied to practical EV systems where a traction machine is available. Eventual deployment of the proposed system will depend on the cost-benefit delivered in the application: The proposed method will reduce the cost of the charging system but will cause the traction machine and inverter to experience a higher effective duty cycle because they will be in-use during driving and charging (whereas in a standard design they would only be used during driving). In addition, during charging, residual winding asymmetry in the traction machine may cause some mechanical vibration at the line frequency. Both factors may slightly reduce component lifespan and should be factored into the design cycle. Future work will focus on the design, modelling and construction of a practical machine in order to explore the MMF cancelling effect and ensure zero torque is produced during charging.

References

[1] M. Yilmaz and P. T. Krein, "Review of Battery Charger Topologies, Charging Power Levels, and Infrastructure for Plug-In Electric and Hybrid Vehicles," *IEEE Trans. Power Electron.*, vol. 28, no. 5, pp. 2151-2169, May 2013.

[2] K. Clement-Nyns, E. Haesen and J. Driesen, "The Impact of Charging Plug-In Hybrid Electric Vehicles on a Residential Distribution Grid," *IEEE Trans. Power Syst.*, vol. 25, no. 1, pp. 371-380, Feb. 2010.

[3] L. Tang and G. J. Su, "A low-cost, digitally-controlled charger for plug-in hybrid electric vehicles," in *Proc. IEEE Energy Convers. Congr. Expo.*, Sep. 2009, pp. 3923–3929.

[4] S. Haghbin *et al*., "Integrated chargers for EV's and PHEV's: examples and new solutions," " in Proc. XIX ICEM, Sep. 6–8, 2010, pp. 1–6.

[5] C. Shi, Y. Tang and A. Khaligh, "A Single-Phase Integrated Onboard Battery Charger Using Propulsion System for Plug-in Electric Vehicles," *IEEE Trans. Veh. Technol.*, vol. 66, no. 12, pp. 10899-10910, Dec. 2017.

[6] A. Kuperman, U. Levy, J. Goren, A. Zafransky and A. Savernin, "Battery Charger for Electric Vehicle Traction Battery Switch Station," *IEEE Trans. Ind. Electron.*, vol. 60, no. 12, pp. 5391-5399, Dec. 2013.

[7] P. T. Krein and R. S. Balog, "Cost-effective hundred-year life for singlephase inverters and rectifiers in solar and LED lighting

applications based on minimum capacitance requirements and a ripple power port," *Appl. Power Electron. Conf., APEC*, pp. 620–625, 2009.
[8] J. Baek, W. Choi and B. Cho, "Digital Adaptive Frequency Modulation for Bidirectional DC–DC Converter," *IEEE Trans. Ind. Electron.*, vol. 60, no. 11, pp. 5167-5176, Nov. 2013.
[9] X. Cao, Q. Zhong and W. Ming, "Ripple Eliminator to Smooth DC-Bus Voltage and Reduce the Total Capacitance Required," *IEEE Trans. Ind. Electron.*, vol. 62, no. 4, pp. 2224-2235, Apr. 2015.
[10] H. Wen, W. Xiao, X. Wen and P. Armstrong, "Analysis and Evaluation of DC-Link Capacitors for High-Power-Density Electric Vehicle Drive Systems," *IEEE Trans. Veh. Technol.*, vol. 61, no. 7, pp. 2950-2964, Sept. 2012
[11] W. Chen and S. Hui, "Elimination of an electrolytic capacitor in AC/DC light-emitting diode (LED) driver with high input power factor and constant output current," *IEEE Trans. Power Electron*., vol. 27, no. 3, pp. 1598–1607, Mar. 2012.
[12] X. Du, L. Zhou, H. Lu, and H.-M. Tai, "DC link active power filter for three-phase diode rectifier," *IEEE Trans. Ind. Electron*., vol. 59, no. 3, pp. 1430–1442, Mar. 2012.
[13] Q. C. Zhong, W. L. Ming, X. Cao, and M. Krstic, "Reduction of DC-bus voltage ripples and capacitors for single-phase PWM-controlled rectifiers," in *Proc. IEEE IECON*, 2012, pp. 708–713.
[14] S. Li, G.-R. Zhu, S.-C. Tan, and S. Hui, "Direct AC/DC Rectifier With Mitigated Low-Frequency Ripple Through Inductor-Current Waveform Control," *IEEE Trans. Power Electron.*, vol. 30, no. 8, pp. 4336-4348, Aug. 2015.
[15] H. Wu, S. Wong, C. K. Tse and Q. Chen, "Control and Modulation of Bidirectional Single-Phase AC–DC Three-Phase-Leg SPWM Converters With Active Power Decoupling and Minimal Storage Capacitance," *IEEE Trans. Power Electron.*, vol. 31, no. 6, pp. 4226-4240, Jun. 2016.
[16] R. Wang *et al*., "A High Power Density Single-Phase PWM Rectifier With Active Ripple Energy Storage," *IEEE Trans. Power Electron.*, vol. 26, no. 5, pp. 1430-1443, May 2011.
[17] Y. Tang, F. Blaabjerg and P. C. Loh, "Decoupling of fluctuating power in single-phase systems through a symmetrical half-bridge circuit," " in *Proc. IEEE Appl. Power Electron. Conf. Expo.*, 2014, pp. 96–102.
[18] M. A. Vitorino, R. Wang, M. B. d. R. Corrêa and D. Boroyevich, "Compensation of DC-Link Oscillation in Single-Phase-to-Single-Phase VSC/CSC and Power Density Comparison," *IEEE Trans. Ind. Appl.*, vol. 50, no. 3, pp. 2021-2028, May./Jun. 2014.
[19] T. Shimizu, Y. Jin and G. Kimura, "DC ripple current reduction on a single-phase PWM voltage-source rectifier," *IEEE Trans. Ind. Appl.*, vol. 36, no. 5, pp. 1419-1429, Sept./Oct. 2000.
[20] M. Su, P. Pan, X. Long, Y. Sun and J. Yang, "An Active Power-Decoupling Method for Single-Phase AC–DC Converters," *IEEE Trans. Ind. Informat.*, vol. 10, no. 1, pp. 461-468, Feb. 2014.
[21] T. Larsson and S. Ostlund, "Active DC link filter for two frequency electric locomotives," in *Proc. Electri. Railways United Eur. Conf.*, Mar. 1995, pp. 97–100.
[22] R. Pinto, M. Cosetin, M. Silva, G. Denardin, J. Fraytag, A. Campos, and R. Prado, "Compact emergency lamp using power LEDs," *IEEE Trans. Ind. Electron.*, vol. 54, no. 4, pp. 1728–1738, Jun. 2012.
[23] R. Hou and A. Emadi, "Applied Integrated Active Filter Auxiliary Power Module for Electrified Vehicles With Single-Phase Onboard Chargers," *IEEE Trans. Power Electron.*, vol. 32, no. 3, pp. 1860-1871, Mar. 2017.
[24] R. Hou and A. Emadi, "Dual active bridge-based full-integrated active filter auxiliary power module for electrified vehicle applications with single-phase onboard chargers," in *Proc. IEEE Appl. Power Electron. Conf. Expo.*, Long Beach, CA, USA, Mar. 2016, pp. 1300–1306.
[25] R. Hou and A. Emadi, "A Primary Full-Integrated Active Filter Auxiliary Power Module in Electrified Vehicles With Single-Phase Onboard Chargers," *IEEE Trans. Power Electron*., vol. 32, no. 11, pp. 8393-8405, Nov. 2017.
[26] S. Haghbin *et al*., "An integrated charger for plug-in hybrid electric vehicles based on a special interior permanent magnet motor," in *Proc. IEEE Veh. Power Propulsion Conf.*, Sep. 2010, pp. 1–6.
[27] S.Lacroix, E.Laboure and M.Hilairet, "An integrated fast battery charger for Electric Vehicle," in *Proc. IEEE Veh. Power Propulsion Conf.*, Sep. 2010, pp. 1–6.
[28] Chapman S J. Electric Machinery Fundamentals[M]. McGraw-Hill Book Co, 1985.



Yun Zhang (M'13-SM'18) was born in Jiangsu, China, in 1980. He received the B.S. and M.S. degrees in electrical engineering from the Harbin University of Science and Technology, Harbin, China, in 2003 and 2006, respectively, and the Ph.D. degree in electrical engineering from the Harbin Institute of Technology, Harbin, China, in 2010.

In 2010, he joined the Tianjin University, Tianjin, China, as a Lecturer in the School of Electrical and Information Engineering, where he is currently a Professor of Power Electronics. From December 2016 to December 2017, he was an Academic Visitor with the Power Electronics, Machines and Control (PEMC) Group at the University of Nottingham, Nottingham, U.K.. His current research interests include topologies, modulation, and control strategies of power converters for electric vehicles and microgrids.

Dr. Zhang is an Associate Editor of the JOURNAL OF POWER ELECTRONICS.



Jian Fang was born in Anhui, China. He received the B.S. degree in electrical engineering from Anhui University, Hefei, China, in 2017. He is currently working toward the M.S. degree in electrical engineering from Tianjin University, Tianjin, China in 2017.

His current research interests include ac-dc converters and isolated dc-dc converters for electric vehicles.



Fei Gao received his M.Sc. degree in Electrical Engineering from Shanghai Jiao Tong University, Shanghai, China, in 2010. He received his Ph.D. degree in Electrical Engineering for his work on control and stability analysis of more electric aircraft electrical power systems from the PEMC Research Group, University of Nottingham, Nottingham, UK, in 2016.

From Mar. 2010 to Sep. 2012, he has worked in Jiangsu Electric Power Research Institute, Nanjing, State Grid Corporation of China. From 2016 to 2019, he has been with Energy and Power Group, University of Oxford, UK as a postdoctoral researcher. Since July 2019 he joined Shanghai Jiao Tong University as an associate professor. His current research interests include modelling, control, power management and stability of microgrids and more electric transportation systems. Dr. Gao won the European Union Clean Sky Best PhD Award in 2017.



Tianbao Song was born in Shandong, China. He received the B.S. degree in electrical engineering from China University of Mining and Technology, Xuzhou, China, in 2017. He is currently working toward the PH.D. degree in electrical engineering from Tianjin University, Tianjin, China in 2017.

His current research interests include ac-dc converters for electric vehicles.



Shenghan Gao was born in Anhui, China. She received her B.S. degree in North China University of Technology, Beijing, China, in 2018. She started pursing her M.S. degree in Electrical Engineering from the Tianjin University, Tianjin, China, in 2018.

Her current research interests include dc-dc converters, and energy management of electric vehicles.



Daniel J. Rogers (M'09) received the M.Eng. and Ph.D. degrees in electrical and electronic engineering from Imperial College London, London, U.K., in 2007 and 2011 respectively. He is an Associate Professor in the Department of Engineering Science at the University of Oxford, UK. He conducts research in collaboration with industry and is an investigator on UK EPSRC research projects in the areas of power electronics, grid-scale energy storage, microgrids and HVDC transmission. Dan's research interests include the use of medium- and large-scale power electronic systems to create flexible electrical networks that take advantage of a diverse range of generation and storage technologies.